Article type: Full Paper

Epitaxy of Layered Orthorhombic SnS-$SnS_xSe_{(1-x)}$ Core-Shell Heterostructures with Anisotropic Photoresponse

Jing Xia, Dandan Zhu, Xuanze Li, Lei Wang, Lifeng Tian, Jing Li, Jingyuan Wang, Xing Huang, and Xiang-Min Meng**

J. Xia, D. D. Zhu, X. Z. Li, L. Wang, L. F. Tian, J. Li, J. Y. Wang, Prof. X. M. Meng
Key Laboratory of Photochemical Conversion and Optoelectronic Materials, Technical Institute of Physics and Chemistry, Chinese Academy of Sciences, Beijing, 100190, P. R. China
E-mail: mengxiangmin@mail.ipc.ac.cn

Dr. X. Huang
Inorganic Department, Fritz Haber Institute of Max Planck Society, Faradayweg 4-6, 14195, Berlin, Germany
E-mail: xinghuang0214@mail.ipc.ac.cn

Keywords: physical vapor deposition, epitaxy, van der Waals crystal, core-shell heterostructure, anisotropic photoresponse

Abstract: Vertical and in-plane heterostructures based on van der Waals (vdW) crystals have drawn rapidly increasing attention owning to the extraordinary properties and significant application potential. However, current heterostructures are mainly limited to vdW crystals with a symmetrical hexagonal lattice, and the heterostructures made by asymmetric vdW crystals are rarely investigated at the moment. In this contribution, we report for the first time the synthesis of layered orthorhombic SnS-$SnS_xSe_{(1-x)}$ core-shell heterostructures with well-defined geometry via a two-step thermal evaporation method. Structural characterization reveals that the heterostructures of SnS-$SnS_xSe_{(1-x)}$ are in-plane interconnected and vertically stacked, constructed by $SnS_xSe_{(1-x)}$ shell heteroepitaxially growing on/around the pre-synthesized SnS flake with an epitaxial relationship of $(303)_{SnS}//(033)_{SnSxSe(1-x)}$, $[010]_{SnS}//[100]_{SnSxSe(1-x)}$. On the basis of detailed morphology, structure and composition characterizations, a growth mechanism involving heteroepitaxial growth, atomic diffusion, as well as thermal thinning is proposed to

illustrate the formation process of the heterostructures. In addition, a strong polarization-dependent photoresponse is found on the device fabricated using the as-prepared SnS-$SnS_xSe_{(1-x)}$ core-shell heterostructure, enabling the potential use of the heterostructures as functional components for optoelectronic devices featured with anisotropy.

1. Introduction

Heterostructures are important functional units for modern electronic and optoelectronic devices such as bipolar transistors, light-emitting diodes, laser diodes, and photovoltaic cells.[1-4] They are formed by combining two or more materials with different band gaps. With the thriving of two-dimensional (2D) layered materials, two types of heterostructures composed of van der Waals (vdW) crystals have recently attracted considerable attention, namely, vertical heterostructures and in-plane heterostructures.[5-10] Generally, the former can be fabricated by vertically stacking different 2D layered materials on top of each other despite the existence of large lattice mismatch, such as the reported graphene-MoS_2,[11, 12] graphene-WS_2-graphene[13] and graphen-GaSe vertical heterostructures.[14] In contrast, the latter are made by laterally stitching different 2D layered materials, exampled as the graphene-BN,[15, 16] MoS_2-WS_2[17, 18] and $MoSe_2$-WSe_2 in-plane heterostructures.[19] Despite the different configuration, there is a common feature among those heterostructures that they are all made of vdW crystals with a symmetrical hexagonal structure. However, heterostructures based on asymmetric layered materials, such as SnSe and SnS with an orthorhombic structure, are rarely investigated. It has been studied that IV-VI layered metal monochalcogenides can display a marked anisotropy in optical, electronic and thermoelectric properties.[20-24] For example, we have investigated orthorhombic SnS flakes using angle-resolved polarized Raman spectroscopy

and found that they show a strong anisotropic Raman response, which can be used to determine the crystal orientation of SnS using Raman spectroscopy.[21] Additionally, Huang' group studied electrical properties of SnS and SnSe, and found that they have anisotropic electrical conductivities due to the different effective masses of holes and electrons along a, b and c axes.[23] In this regard, synthesis of heterostructures composed of asymmetric vdW components is highly desirable. Thus heterostructures may offer unprecedented opportunities to explore new properties and develop novel functional devices unachievable using the conventional materials with a symmetrical structure.

In this paper, we report the epitaxial growth of orthorhombic SnS-$SnS_xSe_{(1-x)}$ core-shell heterostructures using a two-step PVD method. Structural characterizations such as X-ray diffraction (XRD) and transmission electron microscopy (TEM) were utilized to investigate the crystal structure of the products and the epitaxial relationship between the $SnS_xSe_{(1-x)}$ shell and the SnS core flake. It was found that the SnS-$SnS_xSe_{(1-x)}$ core-shell heterostructure is an integration of vertical heterostructure and in-plane heterostructure, which consists of SnS flake with $SnS_xSe_{(1-x)}$ shell heteroepitaxially growing on/around it. A growth model was proposed to illustrate the formation process of the layered SnS-$SnS_xSe_{(1-x)}$ core-shell heterostructures, which involves heteroepitaxial growth, sulphur diffusion, as well as thermal evaporation thinning processes. In addition, photodetector made by the SnS-$SnS_xSe_{(1-x)}$ core-shell heterostructures exhibited a strong anisotropic photoresponse due to the structural characteristic of orthorhombic crystals, enabling the potential use of the heterostructures as building blocks for new functional optoelectronic devices.

2. Results and Discussion

Layered SnS-$SnS_xSe_{(1-x)}$ core-shell heterostructures were synthesized using a simple two-step PVD method. Firstly, large-scale 2D SnS flakes were grown on fluorophlogopite mica substrates.[21] Optical image (Figure S1a) and AFM image (Figure S1b) reveal that the as-synthesized SnS flakes mainly show truncated rhombic shapes with the lateral size ranging from several to tens of microns and the thickness of about 67 nm. Structural characterizations including XRD pattern (Figure S1c) and TEM (Figure S1d and e) confirm that these 2D flakes crystalize into an orthorhombic crystal structure (space group = Pbnm; a = 0.4329 nm, b = 1.1192 nm and c = 0.3984 nm; PDF: 39-0354), and grow preferably along the b axis direction with (010) as the basal plane. Additionally, Raman spectroscopy was also performed to confirm that the as-grown flakes are indeed SnS, as shown in Figure S1f. Subsequently, the pre-synthesized SnS/mica was used as the receiving substrates for the growth of SnS-$SnS_xSe_{(1-x)}$ core-shell heterostructures, which is schematically illustrated in **Figure 1**a. The growth of SnS-$SnS_xSe_{(1-x)}$ core-shell heterostructures is similar to the PVD growth of SnS flakes. The differences are (i) SnSe powder replaced SnS powder as the source material, (ii) SnS/mica was adopted as the substrates, (iii) synthesis conditions of the core-shell heterostructures changed sightly. More experimental details can be found in the Experimental Section.

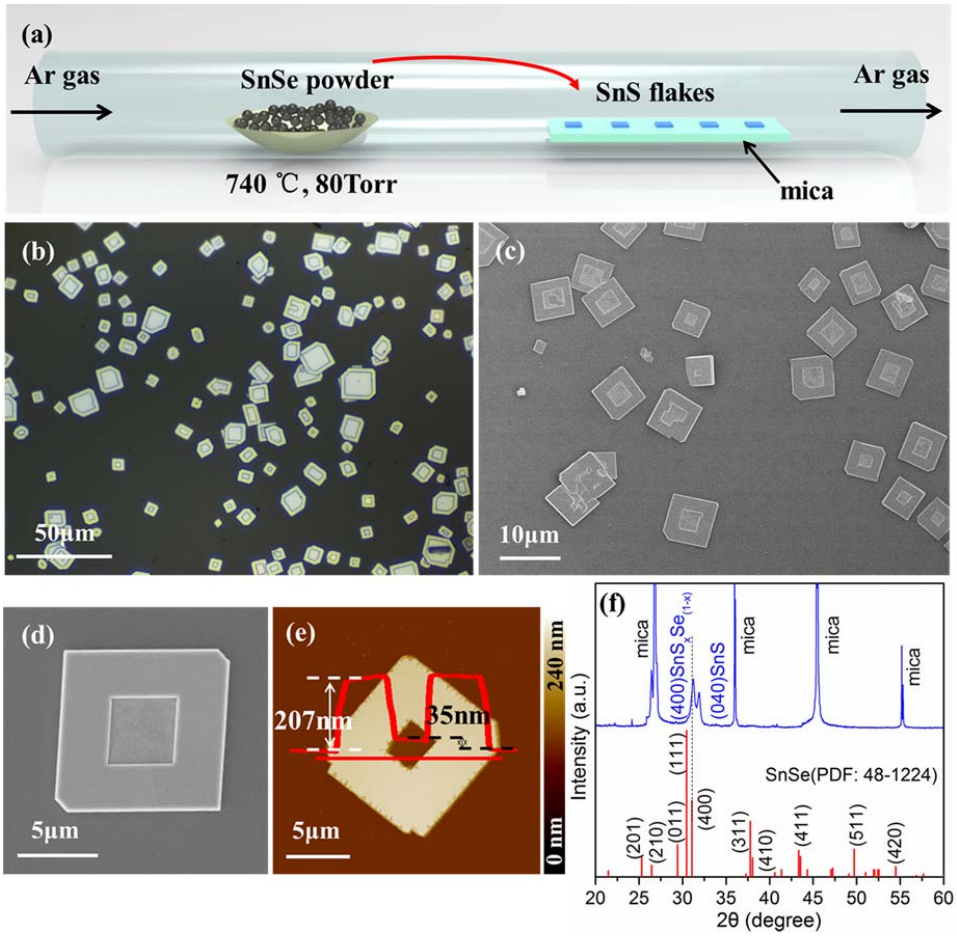

Figure 1. a) Schematic diagram for PVD growth of layered SnS-$SnS_xSe_{(1-x)}$ core-shell heterostructures. b) Optical and c) SEM images of the SnS-$SnS_xSe_{(1-x)}$ core-shell heterostructures. d) SEM image of a representative core-shell heterostructure which exhibits an approximately rhombic shape with a noticeable rhombus pit at the central regions. e) AFM image and height profile of a core-shell heterostructure. f) XRD patterns of the SnS-$SnS_xSe_{(1-x)}$ core-shell heterostructures (blue) and SnSe (red; PDF: 48-1224).

The product obtained in the second deposition process was firstly characterized using optical microscopy and scanning electron microscopy (SEM), as shown in Figure 1b and c. It can be clearly seen that the as-grown flakes mainly exhibit truncated rhombic shapes

with the lateral size of several microns to a dozen microns. The morphology of these flakes is very similar to that of the pre-synthesized 2D SnS flakes except for a noticeable rhombus pit at the center, as exhibited in Figure 1d. The edges of the truncated rhombic flake are observed to be parallel to those of the central rhombus pit, implying the existence of a high-oriented growth in the as-synthesized flakes. To determine the height information of the flakes, AFM characterization was performed. As displayed in Figure 1e, the thickness of the sample from Figure 1b is measured to be about 207 nm, and the thickness of the central rhombus pit is about 35 nm which is smaller than that of the pre-grown SnS. XRD characterization was also carried out to study the phase structure of the product and the result is exhibited in Figure 1f. Compared with the XRD pattern of the 2D SnS flakes (Figure S1c), a new diffraction peak at 31.25° is observed, which is close to the characteristic diffraction peak at 31.081° of orthorhombic SnSe (space group = Pnma; a = 1.1498 nm, b = 0.4153 nm and c = 0.444 nm; PDF: 48-1224).

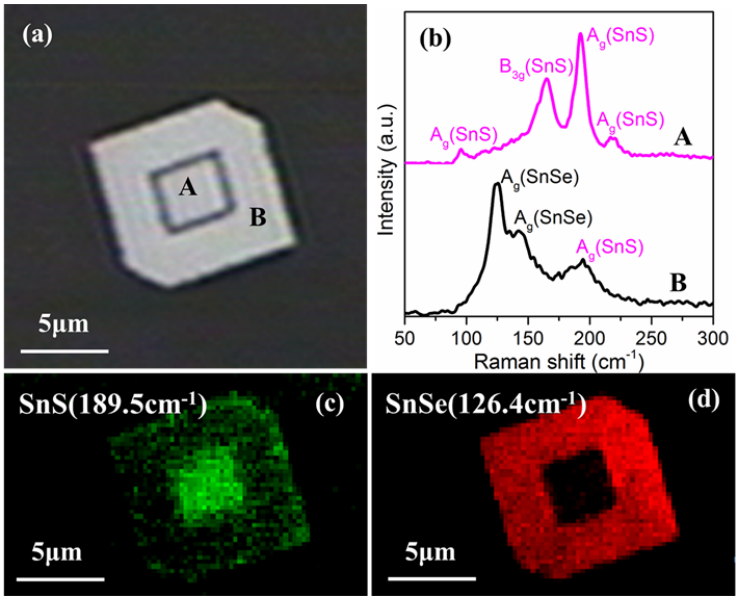

Figure 2. a) Optical image of a SnS-$SnS_xSe_{(1-x)}$ core-shell heterostructure. b) Raman spectra collected from the marked A and B regions, respectively. c, d) Raman intensity maps of the Raman modes at 189.5 cm^{-1} (SnS) and 126.4 cm^{-1} (SnSe), respectively.

Raman spectroscopy was also used to investigate the optical characteristics of the heterostructures with a 532 nm laser. **Figure 2**a displays an optical image of a truncated rhombic sample for Raman characterization. As shown in Figure 2b, four characteristic Raman peaks located at 94.8 cm^{-1}, 160.1cm^{-1}, 189.5 cm^{-1} and 220 cm^{-1} can be clearly observed in the Raman spectrum collected from region A. The Raman peak at 160.1cm^{-1} corresponds to the B_{3g} Raman mode of SnS, and the other three peaks belong to the A_g modes of SnS.[25] For Raman spectrum collected from the region B, both of the Raman peaks at 126.4 cm^{-1} and 145 cm^{-1} can be attributed to the A_g modes of SnSe, and the peak at 189.5 cm^{-1} is related to the A_g mode of SnS.[25, 26] Raman intensity maps of 189.5 cm^{-1} (A_g mode for SnS) and 126.4 cm^{-1} (A_g mode for SnSe) are also shown in Figure 2c and d, respectively. It can be found that the region A only show Raman signal of SnS, while singles of both SnS and SnSe appear in the region B of the sample, which is consistent with the Raman spectroscopy in Figure 2b. These results indicate that the sample in the rhombus pit region is SnS, while it is composed of $SnS_xSe_{(1-x)}$ alloy in the outer region B.

Energy dispersive X-ray spectroscopy (EDX) in scanning transmission electron microscopy (STEM) mode was used to probe the composition of the product. **Figure 3**a exhibits an annular dark-field STEM (ADF-STEM) image of a flake. The heavier contrast of the border than that of the central region can be ascribed to the large differences in thickness and atomic number. Figure 3b-d shows the corresponding EDX elemental maps of the flake. For the convenience of

description, the flake is defined into three parts marked by A, B and C, as shown in Figure 3c. It can be clearly seen that the border regions (A and B) consist of Sn, S and Se elements, while the central rhombic region (C) only shows weak signals of Sn and S. These results indicate that this flake is made of SnS core partially covered with $SnS_xSe_{(1-x)}$, as confirmed by the EDX maps of a cross section sample (Figure S2). Particularly, it is found that the intensity of S in regions A and C is weaker than that in region B (Figure 3c and e), while the intensity of Sn in regions A and B is in close proximity (Figure 3b and e). In consideration of the uniform thickness and high crystallinity of the pre-synthesized 2D SnS flakes (Figure S1), it is logical to infer that the S signal in region A results from the diffusion of S in the bottom SnS flake. The reduced S signal in region C compared to that in region B is attributed to the thinner thickness of the region C arising from the thermal evaporation thinning of the SnS flake at the relatively high temperature (740 °C). As for S in region B, the formation of $SnS_xSe_{(1-x)}$ overlayer could effectively restrain thermal evaporation of the bottom SnS flake, thus showing high-intensity S signal in region B. In fact, it has been reported that S-Se exchange is an effective method to obtain alloys and heterostructures, and the thermal thinning can be used to prepare ultrathin 2D layered materials.[27-31] In a word, the as-grown flakes can be regarded as a combination of lateral and vertical heterostructures of SnS-$SnS_xSe_{(1-x)}$. To make it simple, we name them as SnS-$SnS_xSe_{(1-x)}$ core-shell heterostructures.

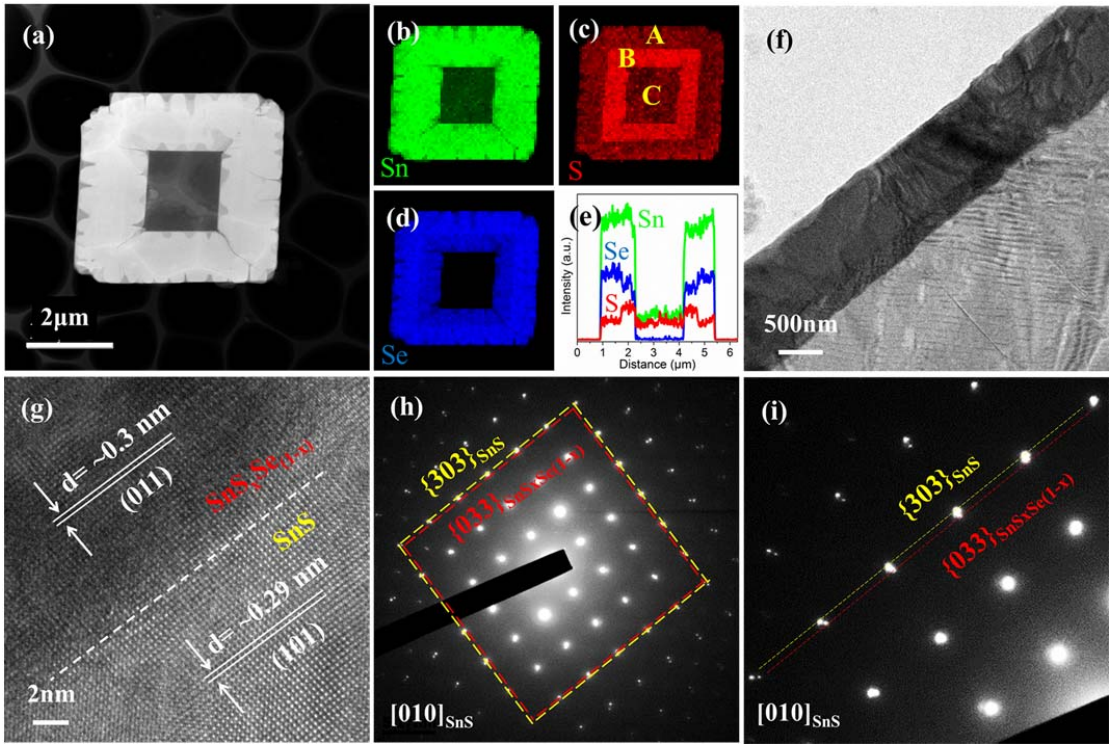

Figure 3. a) ADF-STEM image of a SnS-$SnS_xSe_{(1-x)}$ core-shell heterostructure. b-d) EDX elemental maps and e) EDX line scan profiles showing the spatial distribution of Sn, S and Se across the heterostructure. For the convenience of expression, the flake was defined in three regions marked by A, B and C in Figure 3c. f) Bright-field TEM image of the interface of a thin SnS-$SnS_xSe_{(1-x)}$ core-shell heterostructure. g) HRTEM image of the interface of the heterostructure. h) SAED pattern along $[010]_{SnS}$ zone axis and i) the partial enlarged view of the SAED pattern.

In order to investigate the atomic structure of the SnS-$SnS_xSe_{(1-x)}$ core-shell heterostructures, high-resolution TEM (HRTEM) and selected area electron diffraction (SAED) techniques were used. Figure 3f exhibits a bright-field TEM image of the interface of a thin SnS-$SnS_xSe_{(1-x)}$ core-shell heterostructure. Corresponding HRTEM image is displayed in Figure 3g. It can be seen that SnS core and $SnS_xSe_{(1-x)}$ shell both

show clear 2D rhombic fringes. In the core region, the lattice fringes with d-spacing of about 0.29 nm agree well with {101} planes of orthorhombic SnS (PDF: 39-0354). As for $SnS_xSe_{(1-x)}$, the distance is measured to be about 0.3 nm, which is close to the distance of {011} planes of $SnS_{0.29}Se_{0.71}$ (space group = Pnma; a = 1.1409 nm, b = 0.41 nm and c = 0.4407 nm), calculated using Vegard's law and the lattice parameters of orthorhombic SnS (PDF: 39-0354) and SnSe (PDF: 48-1224).[28, 32] Additionally, the (101) plane of SnS is found to be parallel to the (011) plane of $SnS_{0.29}Se_{0.71}$, implying an epitaxial relationship existed in the heterostructure. Figure 3h shows the corresponding SAED pattern of the core/shell heterostructure. Due to the small difference in lattice constant between SnS and $SnS_{0.29}Se_{0.71}$, it is unable to distinguish them from low-order reflections, such as $\{101\}_{SnS}$ and $\{011\}_{SnS0.29Se0.71}$ (Figure 3h). However, in the high-order reflections, the spots will separate, which allows a chance for identification, as shown in Figure 3i. The enlarged SAED pattern clearly shows two sets of well-aligned rhombic spots, in which the brighter set (yellow dotted line) originates from the SnS, while the darker set (red dotted line) belongs to the $SnS_{0.29}Se_{0.71}$. The good alignment of the two sets of spots offers the clear and convincing evidence that $SnS_{0.29}Se_{0.71}$ was grown epitaxially on the SnS flake. The epitaxial relationship between SnS and $SnS_{0.29}Se_{0.71}$ can be described by $(303)_{SnS}//(033)_{SnS0.29Se0.71}$, $[010]_{SnS}//[100]_{SnS0.29Se0.71}$. More TEM analysis can be found in Figure S3.

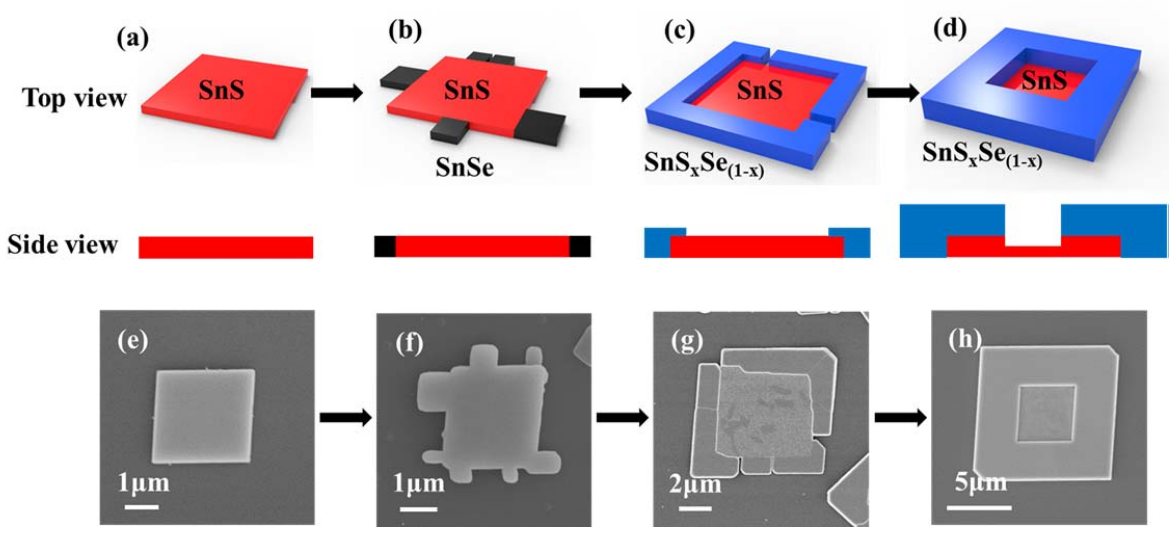

Figure 4. a-d) Schematic diagram illustrating the growth process of a SnS-$SnS_xSe_{(1-x)}$ core-shell heterostructure. e-h) SEM images of the core-shell heterostructures at different growth stages. Note: the heterostructures shown in e-h) were not recorded from the same one.

Understanding the growth mechanism of the SnS-$SnS_xSe_{(1-x)}$ core-shell heterostructure will facilitate a better control in terms of morphology and composition, which, eventually, will drive the development of novel functional devices. According to above experimental results and analyses, we may address that the SnS-$SnS_xSe_{(1-x)}$ core-shell heterostructure is a result of a heteroepitaxial growth of SnSe accompanying with the diffusion of sulfur from SnS, as illustrated in **Figure 4**a-d. At the beginning, gaseous SnSe species, resulted from the sublimation of SnSe powder, are transported downstream to the deposition area where the pre-grown SnS located. Governed by the surface energy, the lateral growth of SnSe occurs preferably on side surfaces of SnS because of the existence of unsaturated Sn and S atoms. Due to the small lattice mismatch between SnSe and SnS, growth of SnSe follows an epitaxial growth manner, as evidenced above. Spontaneously with the SnSe growth, the S^{2-} in the SnS will diffuse into the

grown SnSe and substitute for Se^{2-} to form ternary $SnS_xSe_{(1-x)}$ driven by a thermodynamically process. Over extended time, the epitaxial layer increases both laterally and vertically. When the thickness of $SnS_xSe_{(1-x)}$ exceeds to that of the SnS flake, lateral growth will proceed not only outward but also inward of SnS flake. Consequently, some border regions of the SnS flake are covered by the growing $SnS_xSe_{(1-x)}$, as shown in Figure 3b-e and Figure S2b-d. Due to the relatively high temperature at the grown zone, the uncovered regions of SnS flake will be gradually evaporated, which will lead to the final formation of a rhombus pit in the SnS-$SnS_xSe_{(1-x)}$ core-shell heterostructures (Figure 1e and 4h). Some direct clues for the proposed growth model can be found from the SEM images displayed in Figure 4e-h and S4a-d, which show the morphologies of the flakes grown at different stages. Unlike those conventional heterostructures which can be categorized as either vertical or in-plane heterostructures, the achieved SnS-$SnS_xSe_{(1-x)}$ core-shell heterostructures in the current work can be considered as a mixture of the lateral and vertical heterostructures.[33-36] This special architecture may enable an effective utilization of the building block by providing more junction regions. In particular, the anisotropic layered orthorhombic crystal structure of the heterostructures may offer us new opportunities to develop novel devices based on the anisotropy.

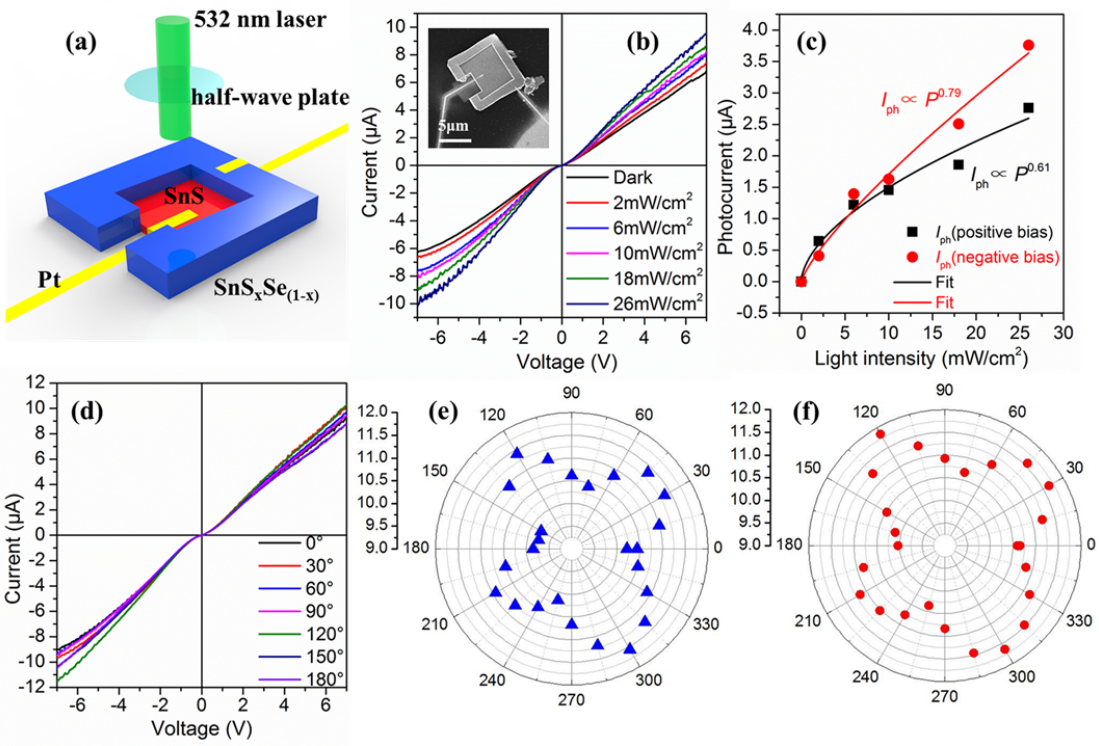

Figure 5. a) Three-dimensional schematic models of the SnS-$SnS_xSe_{(1-x)}$ core-shell heterostructure-based photodetector, the 532 nm laser and the half-wave plate. b) *I-V* curves of the device in the dark and in the presence of 532 nm laser illumination with different light intensities. Inset shows an HIM image of a SnS-$SnS_xSe_{(1-x)}$ core-shell heterostructure photodetector. c) Light intensity dependence of the photocurrent under the bias of positive/negative 7 V. d) *I-V* curves of the device in the presence of 532 nm laser with light intensity of 26 mW/cm^2 and laser polarization angle ranging from 0° to 180°. e, f) Polarization dependence of the current intensity under bias of positive/negative 7 V and light intensity of 26 mW/cm^2.

Next, the optoelectronic properties of the SnS-$SnS_xSe_{(1-x)}$ core-shell heterostructures were investigated. After a small part of the shell of the heterostructure was cut to get a gap using

focused helium ion beam in a helium ion microscope (HIM) system, Pt electrodes were formed via HIM to connect the core and the shell, respectively. Just as displayed in **Figure 5**a, a two-electrode photodetector based on a SnS-$SnS_xSe_{(1-x)}$ core-shell heterostructure was obtained. Figure 5b shows the current (*I*) - voltage (*V*) characteristics of the device (inset in Figure 5b) in the dark and in the presence of 532 nm laser with light intensity varying from 2 to 26 mW/cm^2. The approximate linear behavior of the *I*-*V* plots reveals a good contact between the heterostructure and the Pt electrodes. It is noteworthy that there exists small turn-on voltages at +0.25 V (positive voltage region) and -0.23 V (negative voltage region), which may result from the potential barrier between p-type SnS core and p-type $SnS_xSe_{(1-x)}$ shell. Similar phenomena have been observed in n-n type heterostructures of InAs-Ge and GaAs-Ge.[37, 38] In addition, the large dark current indicates the presence of a high doping concentration in the SnS-$SnS_xSe_{(1-x)}$ core-shell heterostructure, which may be attributed to the formation of massive Sn vacancies during the PVD growth.[39, 40] Under the 532 nm laser illumination, the photocurrent (I_{ph} = $I_{illuminated} - I_{dark}$) increases gradually as the light intensity varies from 2 to 26 mW/cm^2, suggesting a good photoresponse of this device. The dependence of photocurrent I_{ph} to light intensity *P* is plotted in Figure 5c. By fitting the experimental data, the photocurrent I_{ph} can be expressed using the power-law equations $I_{ph} \propto P^{0.61}$ (positive 7V) and $I_{ph} \propto P^{0.79}$ (negative 7V), respectively.[41] The deviation from the ideal slope implies the loss of light energy during the conversion from external light energy to current, which maybe results from the high concentration of vacancies in the heterostructure. [39, 42]

To explore the anisotropic property of the SnS-$SnS_xSe_{(1-x)}$ core-shell heterostructures, polarization-dependent photoresponse measurements were also performed. Figure 5d exhibits the *I*-*V* curves of the device in the presence of 532 nm laser with light intensity of 26 mW/cm^2 and

laser polarization angle ranging from 0° to 180°. It can be clearly seen that the current intensity varies with the change of laser polarization. As displayed in Figure 5e and f, both of the current intensity (under the bias of positive/negative 7 V and the light intensity of 26 mW/cm^2) show a 180° variation period and reach the local maximum when the polarization angle is 30°, 120°, 210° or 300°. The current anisotropy ratio, $\omega = (I_{max} - I_{min})/ (I_{max} + I_{min})$ can be calculated to be about 0.082 and 0.084, respectively. Very recently, it has been demonstrated that SnS possesses strong anisotropy in Raman response, electrical transport and thermal conductivity due to the anisotropic crystal structure.[21-23] In our case, both SnS and $SnS_xSe_{(1-x)}$ have an orthorhombic crystal structure, therefore, it is logical to speculate that the anisotropic photoresponse of the device should be a result of the anisotropic orthorhombic structure of SnS and $SnS_xSe_{(1-x)}$.

3. Conclusion

Layered SnS-$SnS_xSe_{(1-x)}$ core-shell heterostructures have been synthesized on mica substrate by depositing SnSe on the pre-grown SnS flakes using a simple two-step PVD method. The $SnS_xSe_{(1-x)}$ was found to heteroepitaxially grow on/around the SnS flake. The epitaxial relationship was identified to be $(303)_{SnS}//(033)_{SnSxSe(1-x)}$, $[010]_{SnS}//[100]_{SnSxSe(1-x)}$. The presence of S in the exitaxial layer is because of the diffusion of S from SnS driven by a thermal dynamic process. A possible growth mechanism containing heteroepitaxial growth, atomic diffusion and thermal evaporation thinning was proposed to illustrate the formation process of the layered SnS-$SnS_xSe_{(1-x)}$ core-shell heterostructures. Furthermore, a two-electrode photodetector based on the SnS-$SnS_xSe_{(1-x)}$ core-shell heterostructures was fabricated and the device showed a strong anisotropic photoresponse, which makes the heterostructure a promising candidate for developing novel functional optoelectronic devices.

4. Experimental Section

Synthesis of 2D SnS flakes: 2D SnS flakes were synthesized by evaporation of solid SnS powder precursor in a one-inch-diameter quartz heated by a high-temperature horizontal tube furnace. In a typical growth, a ceramic boat containing 0.1 g SnS powder was placed at the heating zone center of the tube furnace. A few newly cleaved fluorophlogopite mica sheets were adopted as the receiving substrates and put downstream with a distance of about 8-20 cm from the heating zone center. The furnace chamber was pumped down to expel the air and then filled with high-purity Ar gas to the pressure of about 80 Torr. Next, the furnace was heated to 700 °C with a rate of 20 °C/min and kept for 10 minutes. The furnace was naturally cooled back to room temperature. In the whole process, Ar gas was used as the carrier gas with a flow rate of 60 sccm.

Synthesis of SnS-$SnS_xSe_{(1-x)}$ core-shell heterostructures: SnS-$SnS_xSe_{(1-x)}$ core-shell heterostructures were synthesized by evaporation of solid SnSe powder precursor in the same furnace. In a typical growth, a ceramic boat containing 0.1 g SnSe powder was put at the heating zone center of the tube furnace. A few mica sheets with SnS flakes were used as the depositing substrates and put downstream with a distance of about 8-20 cm from the heating zone center. The furnace chamber was pumped down to expel the air and then filled with high-purity Ar gas to the pressure of about 80 Torr. Next, the furnace was heated to 740 °C with a rate of 20 °C/min and kept for 15 minutes before it was naturally cooled back to room temperature. In the whole process, Ar gas was used as the carrier gas with a flow rate of 60 sccm.

Characterization: SEM and optical images was obtained in scanning electron microscope (Hitachi S4800 field-emission microscope) and optical microscope (Nikon Inverted Microscope Eclipse Ti-U with a CCD of Nikon Digital Sight). Thickness profile was determined in an atomic force microscope of Bruker Mutimode 8. X-ray diffraction pattern of the sample was recorded using a Bruker D 8 Focus powder X-ray diffractometer using Cu-Kα radiation (λ = 1.5418 Å). Raman characterization was taken in Nanophoton Raman-11 Raman microscope with a 532 nm laser. For TEM characterization, an ultrathin carbon film supported on copper grids was used. The method for transferring SnS and $SnS/SnS_xSe_{(1-x)}$ flakes is similar to that reported in our previous work. The atomic structure of the sample was investigated using JEOL JEM-2100F. STEM image and EDX elemental maps were taken on an aberration-corrected JEOL JEM-ARM200CF operated at 200 kV. The microscope is equipped with a high angle Silicon Drift EDX detector with the solid angle of up to 0.98 steradians from a detection area of 100 mm^2.

Device fabrication and measurements: Photodetector based on the $SnS\text{-}SnS_xSe_{(1-x)}$ core-shell heterostructure was directly fabricated on the mica substrates. In brief, coarse electrodes were made using a shadow mask method and Pt contacts were obtained in a helium ion microscope (Carl Zeiss ORION NanoFab with three beam system). The device was annealed at 200 ℃ for 2 h in Ar atmosphere to reduce resistance. Photoresponse measurements were carried out using a Lakeshore probe station and a Keithley-4200 SCS semiconductor parameter analyser under atmosphere environment. A 532 nm laser was adopted for the illumination. A laser attenuator and a laser power meter were used to get different intensities of the incident beam. To obtain different polarized irradiation, a half-

wave plate was inserted into the optical path and rotated while remaining the light intensity unchanged.

Supporting Information
Supporting Information is available from the Wiley Online Library or from the author.

Acknowledgements
We thank the financial supports from the "Strategic Priority Research Program" of Chinese Academy of Sciences (Grant No. XDA09040203), 973 Project (Grant No. 2012CB932401) and Natural Science Foundation of China (Grant No. 61307065, 21401205 and 61307065). Additionally, we thank Mr. Adnan Hammud and Dr. Marc Willinger for cross-sectional TEM sample preparation and technical support, respectively.

Received: ((will be filled in by the editorial staff))
Revised: ((will be filled in by the editorial staff))
Published online: ((will be filled in by the editorial staff))

[1] H. Kroemer, *P. IEEE.* **1982**, *70*, 13.
[2] S. Nakamura, M. Senoh, T. Mukai, *Appl. Phys. Lett.* **1993**, *62*, 2390.
[3] J. Faist, F. Capasso, D. L. Sivco, C. Sirtori, A. L. Hutchinson, A. Y. Cho, *Science* **1994**, *264*, 553.
[4] J. Schrier, D. O. Demchenko, L. W. Wang, *Nano Lett.* **2007**, *7*, 2377.
[5] A. Castellanos-Gomez, *J. Phys. Chem. Lett.* **2015**, *6*, 4280.
[6] C. Tan, H. Zhang, *J. Am. Chem. Soc.* **2015**, *137*, 12162.
[7] A. K. Geim, I. V. Grigorieva, *Nature* **2013**, *499*, 419.
[8] H. Wang, F. C. Liu, W. Fu, Z. Y. Fang, W. Zhou, Z. Liu, *Nanoscale* **2014**, *6*, 12250.
[9] Y. Shi, H. Li, L.-J. Li, *Chem. Soc. Rev.* **2015**, *44*, 2744.
[10] H. Heo, J. H. Sung, G. Jin, J. H. Ahn, K. Kim, M. J. Lee, S. Cha, H. Choi, M. H. Jo, *Adv. Mater.* **2015**, *27*, 3803.
[11] N. Myoung, K. Seo, S. J. Lee, G. Ihm, *ACS Nano* **2013**, *7*, 7021.
[12] Y. M. Shi, W. Zhou, A. Y. Lu, W. J. Fang, Y. H. Lee, A. L. Hsu, S. M. Kim, K. K. Kim, H. Y. Yang, L. J. Li, J. C. Idrobo, J. Kong, *Nano Lett.* **2012**, *12*, 2784.
[13] L. Britnell, R. M. Ribeiro, A. Eckmann, R. Jalil, B. D. Belle, A. Mishchenko, Y. J. Kim, R. V. Gorbachev, T. Georgiou, S. V. Morozov, A. N. Grigorenko, A. K. Geim, C. Casiraghi, A. H. Castro Neto, K. S. Novoselov, *Science* **2013**, *340*, 1311.
[14] X. F. Li, L. Basile, B. Huang, C. Ma, J. W. Lee, I. V. Vlassiouk, A. A. Puretzky, M. W. Lin, M. Yoon, M. F. Chi, J. C. Idrobo, C. M. Rouleau, B. G. Sumpter, D. B. Geohegan, K. Xiao, *ACS Nano* **2015**, *9*, 8078.

[15] Z. Liu, L. L. Ma, G. Shi, W. Zhou, Y. J. Gong, S. D. Lei, X. B. Yang, J. N. Zhang, J. J. Yu, K. P. Hackenberg, A. Babakhani, J. C. Idrobo, R. Vajtai, J. Lou, P. M. Ajayan, *Nat. Nanotechnol.* **2013**, *8*, 119.
[16] L. Liu, J. Park, D. A. Siegel, K. F. McCarty, K. W. Clark, W. Deng, L. Basile, J. C. Idrobo, A.-P. Li, G. Gu, *Science* **2014**, *343*, 163.
[17] X. Q. Zhang, C. H. Lin, Y. W. Tseng, K. H. Huang, Y. H. Lee, *Nano Lett.* **2015**, *15*, 410.
[18] Y. J. Gong, J. H. Lin, X. L. Wang, G. Shi, S. D. Lei, Z. Lin, X. L. Zou, G. L. Ye, R. Vajtai, B. I. Yakobson, H. Terrones, M. Terrones, B. K. Tay, J. Lou, S. T. Pantelides, Z. Liu, W. Zhou, P. M. Ajayan, *Nat. Mater.* **2014**, *13*, 1135.
[19] C. M. Huang, S. F. Wu, A. M. Sanchez, J. J. P. Peters, R. Beanland, J. S. Ross, P. Rivera, W. Yao, D. H. Cobden, X. D. Xu, *Nat. Mater.* **2014**, *13*, 1096.
[20] M. Patel, A. Chavda, I. Mukhopadhyay, J. Kim, A. Ray, *Nanoscale* **2016**, *8*, 2293.
[21] J. Xia, X.-Z. Li, X. Huang, N. Mao, D.-D. Zhu, L. Wang, H. Xu, X.-M. Meng, *Nanoscale* **2016** *8*, 2063.
[22] G. S. Shi, E. Kioupakis, *Nano Lett.* **2015**, *15*, 6926.
[23] R. Q. Guo, X. J. Wang, Y. D. Kuang, B. L. Huang, *Phys. Rev. B* **2015**, *92*. 115202.
[24] L. D. Zhao, S. H. Lo, Y. S. Zhang, H. Sun, G. J. Tan, C. Uher, C. Wolverton, V. P. Dravid, M. G. Kanatzidis, *Nature* **2014**, *508*, 373.
[25] H. R. Chandrasekhar, R. G. Humphreys, U. Zwick, M. Cardona, *Phys. Rev. B* **1977**, *15*, 2177.
[26] S. L. Zhao, H. A. Wang, Y. Zhou, L. Liao, Y. Jiang, X. Yang, G. C. Chen, M. Lin, Y. Wang, H. L. Peng, Z. F. Liu, *Nano Res.* **2015**, *8*, 288.
[27] X. Huang, M. Wang, M.-G. Willinger, L. Shao, D. S. Su, X.-M. Meng, *ACS Nano* **2012**, *6*, 7333.
[28] Y. Myung, D. M. Jang, T. K. Sung, Y. J. Sohn, G. B. Jung, Y. J. Cho, H. S. Kim, J. Park, *ACS Nano* **2010**, *4*, 3789.
[29] D. Rudolph, S. Funk, M. Doeblinger, S. Morkoetter, S. Hertenberger, L. Schweickert, J. Becker, S. Matich, M. Bichler, D. Spirkoska, I. Zardo, J. J. Finley, G. Abstreiter, G. Koblmueller, *Nano Lett.* **2013**, *13*, 1522.
[30] S. Balendhran, J. Z. Ou, M. Bhaskaran, S. Sriram, S. Ippolito, Z. Vasic, E. Kats, S. Bhargava, S. Zhuiykov, K. Kalantar-zadeh, *Nanoscale* **2012**, *4*, 461.
[31] J. Wu, H. Li, Z. Y. Yin, H. Li, J. Q. Liu, X. H. Cao, Q. Zhang, H. Zhang, *Small* **2013**, *9*, 3314.
[32] A. L. Pan, H. Yang, R. B. Liu, R. C. Yu, B. S. Zou, Z. L. Wang, *J. Am. Chem. Soc.* **2005**, *127*, 15692-15693.
[33] S. S. Wang, X. C. Wang, J. H. Warner, *ACS Nano* **2015**, *9*, 5246.
[34] R. Browning, P. Plachinda, P. Padigi, R. Solanki, S. Rouvimov, *Nanoscale* **2016**, *8*, 2143.
[35] F. Withers, O. Del Pozo-Zamudio, A. Mishchenko, A. P. Rooney, A. Gholinia, K. Watanabe, T. Taniguchi, S. J. Haigh, A. K. Geim, A. I. Tartakovskii, K. S. Novoselov, *Nat. Mater.* **2015**, *14*, 301.
[36] M. Y. Li, Y. M. Shi, C. C. Cheng, L. S. Lu, Y. C. Lin, H. L. Tang, M. L. Tsai, C. W. Chu, K. H. Wei, J. H. He, W. H. Chang, K. Suenaga, L. J. Li, *Science* **2015**, *349*, 524.
[37] K. Tomioka, F. Izhizaka, T. Fukui, *Nano Lett.* **2015**, *15*, 7253.
[38] R. L. Anderson, *Solid State Electron.* **1962**, *5*, 341.
[39] P. Sinsermsuksakul, J. Heo, W. Noh, A. S. Hock, R. G. Gordon, *Adv. Energy Mater.* **2011**, *1*, 1116.

[40] A. de Kergommeaux, M. Lopez-Haro, S. Pouget, J.-M. Zuo, C. Lebrun, F. Chandezon, D. Aldakoy, P. Reiss, *J. Am. Chem. Soc.* **2015**, *137*, 9943.
[41] J. Xia, D. Zhu, L. Wang, B. Huang, X. Huang, X.-M. Meng, *Adv. Funct. Mater.* **2015**, *25*, 4255.
[42] Q. S. Wang, M. Safdar, K. Xu, M. Mirza, Z. X. Wang, J. He, *ACS Nano* **2014**, *8*, 7497.

Table of Contents Graphic

Keywords: physical vapor deposition, epitaxy, van der Waals crystal, core-shell heterostructure, anisotropic photoresponse

Epitaxy of Layered Orthorhombic SnS-$SnS_xSe_{(1-x)}$ Core-Shell Heterostructures with Anisotropic Photoresponse

Jing Xia, Dandan Zhu, Xuanze Li, Lei Wang, Lifeng Tian, Jing Li, Jingyuan Wang, Xing Huang, and Xiang-Min Meng**

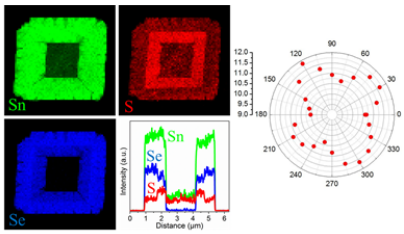

Layered orthorhombic SnS-$SnS_xSe_{(1-x)}$ core-shell heterostructures are successfully synthesized via an epitaxial growth method. Due to the structural characteristic of the components, the heterostructures are able to show a strong polarization-dependent photoresponse, which will facilitate developing novel functional optoelectronic devices beyond conventional materials.